AGU PUBLICATIONS

JGR

Journal of Geophysical Research: Solid Earth

RESEARCH ARTICLE
10.1002/2015JB012417

Key Points:
- Characterization of the time evolution of slip following the 2007 Pisco, Peru, earthquake
- Postseismic relocking of the subduction megathrust revealed by GPS and InSAR data
- Aseismic slip might account for about 50% of the slip budget in the region of Pisco

Supporting Information:
- Supporting Information S1

Correspondence to:
D. Remy,
remy@ird.fr

Citation:
Remy, D., H. Perfettini, N. Cotte, J. P. Avouac, M. Chlieh, F. Bondoux, A. Sladen, H. Tavera, and A. Socquet (2016), Postseismic relocking of the subduction megathrust following the 2007 Pisco, Peru, earthquake, *J. Geophys. Res. Solid Earth*, *121*, doi:10.1002/2015JB012417.

Received 22 JUL 2015
Accepted 28 APR 2016
Accepted article online 3 MAY 2016

Postseismic relocking of the subduction megathrust following the 2007 Pisco, Peru, earthquake

D. Remy[1], H. Perfettini[2], N. Cotte[2], J. P. Avouac[3], M. Chlieh[4], F. Bondoux[1], A. Sladen[4], H. Tavera[5], and A. Socquet[2]

[1]GET/UMR5563 (UPS, CNRS, IRD, CNES); Obs. Midi-Pyrénées, Université P. Sabatier, Toulouse, France, [2]ISTERRE/UMR5275 (UJF, CNRS, IRD); Université Grenoble Alpes, Grenoble, France, [3]Division of Geological and Planetary Science, California Institute of Technology, Pasadena, California, USA, [4]GEOAZUR/UMR7329 (UNSA, CNRS, IRD); Obs. de la Côte d'Azur, Université Nice-Sophia Antipolis, Valbonne, France, [5]Instituto Geofísico del Perú, Ate, Peru

Abstract Characterizing the time evolution of slip over different phases of the seismic cycle is crucial to a better understanding of the factors controlling the occurrence of large earthquakes. In this study, we take advantage of interferometric synthetic aperture radar data and 3.5 years of continuous Global Positioning System (GPS) measurements to determine interseismic, coseismic, and postseismic slip distributions in the region of the 2007, M_w 8.0 Pisco, earthquake, Peru, using the same fault geometry and inversion method. Our interseismic model, based on pre-2007 campaign GPS data, suggests that the 2007 Pisco seismic slip occurred in a region strongly coupled before the earthquake while afterslip occurred in low coupled regions. Large afterslip occurred in the peripheral area of coseismic rupture in agreement with the notion that afterslip is mainly induced by coseismic stress changes. The temporal evolution of the region of maximum afterslip, characterized by a relaxation time of about 2.3 years, is located in the region where the Nazca ridge is subducting, consistent with rate-strengthening friction promoting aseismic slip. We estimate a return period for the Pisco earthquake of about 230 years with an estimated aseismic slip that might account for about 50% of the slip budget in this region over the 0–50 km seismogenic depth range. A major result of this study is that the main asperity that ruptured during the 2007 Pisco earthquake relocked soon after this event.

1. Introduction

A number of studies have shown that Global Positioning System (GPS) and interferometric synthetic aperture interferometry (InSAR) can be used to measure interseismic, coseismic, and postseismic strain at plate boundaries and subduction zones in particular [e.g., *Pritchard and Simons*, 2006; *Subarya et al.*, 2006; *Chlieh et al.*, 2007; *Moreno et al.*, 2010; *Perfettini et al.*, 2010; *Chlieh et al.*, 2011; *Loveless and Meade*, 2011]. These studies have revealed that, in the 0–50 km seismogenic depth range, the frictional properties of the subduction interface are heterogeneous. Based on these findings, the megathrust appears as a patchwork of areas either governed by rate-weakening friction, promoting earthquake nucleation, or by rate-strengthening friction, promoting aseismic slip. A fundamental question is whether those frictional properties are permanent or vary during the seismic cycle.

Here we focus on the spatiotemporal evolution of slip on the megathrust offshore southern Peru revealed by observations of the surface deformation obtained by both GPS and InSAR data before, during, and after the 15 August 2007, Pisco earthquake (Figure 1). This earthquake occurred along the subduction segment located just north of the prominent Nazca ridge which is subducting beneath the South American plate at a convergence rate of about 6 cm/yr [*Kendrick et al.*, 2001]. The rupture initiated north of the city of Pisco and propagated southward below the Paracas Peninsula and offshore before stopping on the northern edge of the Nazca ridge [*Sladen et al.*, 2010]. The Nazca ridge separates the central and southern Peru subduction segments that have been affected by numerous great subduction megathrust earthquakes with moment magnitude M_w equal or higher than 8.5 in 1604, 1664, 1687, 1746, and 1868 [*Dorbath et al.*, 1990]. Large megathrust earthquakes ($M_w > 7.5$) also occur frequently in the subduction segment located north of the Nazca ridge such as the 1940 (M_w 7.8), 1966 (M_w 8.0), 1974 (M_w 7.9), and 2007 (M_w 8.0) earthquakes or south of the Nazca ridge such as the 1942 (M_w8.1), 1996 (M_w 7.7), and 2001 (M_w 8.4) earthquakes [*Dorbath et al.*, 1990; *Pritchard et al.*, 2007]. Apparently, no historical event ruptured through the segment corresponding to the subduction of the Nazca ridge, suggesting that this area could be a permanent barrier to earthquake rupture propagation [*Dorbath et al.*, 1990; *Perfettini et al.*, 2010; *Chlieh et al.*, 2011].

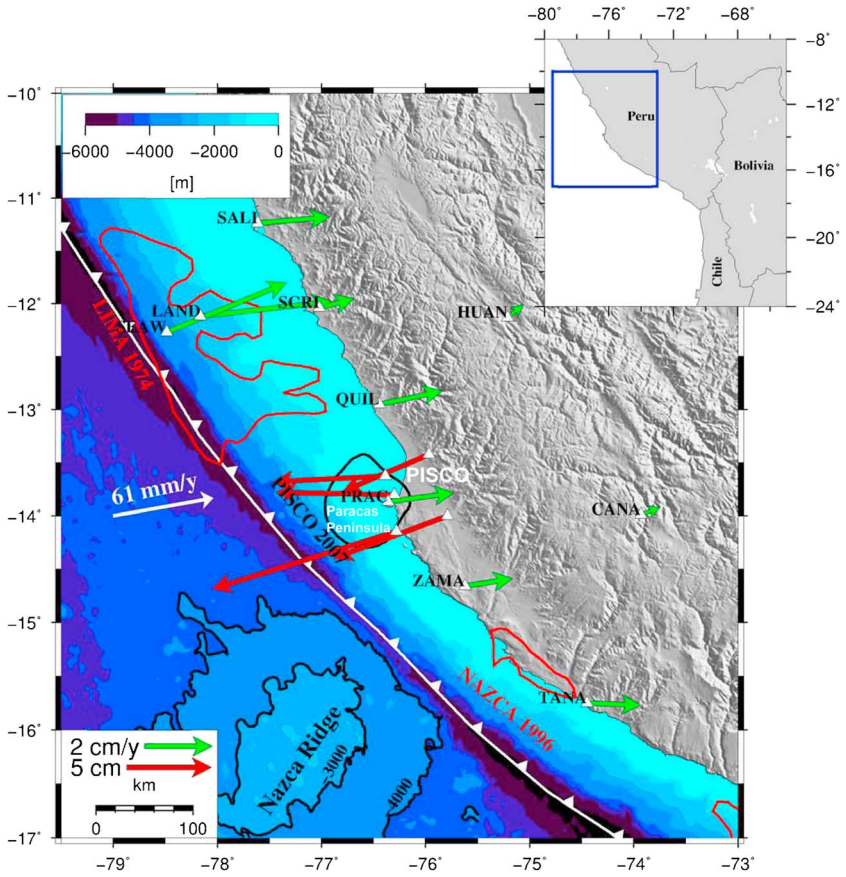

Figure 1. Reference map of the study area in Peru (delimited by a blue box in the inset map). The relative Nazca-South American convergence rate and direction determined by *Kendrick et al.* [2003] are represented by a white arrow. The white barbed line shows the location of the trench. Representative bathymetric contours of the Nazca ridge are shown in black heavy lines. Approximate rupture areas for the M_w8.0, 1974 Lima [*Langer and Spence*, 1995] and the M_w7.7, 1996 Nazca earthquakes [*Pritchard et al.*, 2007] are indicated by red contours. The rupture area of the M_w8.0, 2007 Pisco earthquake from this study is shown in black. Green arrows show the interseismic GPS velocities in the South American reference frame before the 2007 Pisco earthquake as compiled by *Chlieh et al.* [2011]. Red arrows show the horizontal surface displacement observed by the network of five GPS stations from 20 to 500 days after the main shock.

The detailed characteristics of the seismic source associated with the 2007 Pisco earthquake were described by *Sladen et al.* [2010] based on individual and joint inversions of seismic and InSAR data. The source time function shows a clear distribution with two peaks, isolated by 60 s of seismic quiescence, corresponding to the rupture of two main asperities. Several other published coseismic slip models yielded a more homogeneous slip distribution involving the rupture of a single asperity [*Motagh et al.*, 2008; *Pritchard and Fielding*, 2008; *Biggs et al.*, 2009; *Chlieh et al.*, 2011]. Tsunami modeling performed considering the three coseismic slip distributions given by *Sladen et al.* [2010] (obtained considering teleseismic and InSAR data separately or jointly) showed that the single asperity model was in better agreement with the tsunami data than the slip models obtained considering teleseismic data (separately or combined to the InSAR data) [*Ioualalen et al.*, 2012].

Perfettini et al. [2010] pieced together the various phases of the seismic cycle in the area of the Pisco earthquake. To characterize the postseismic phase, they used data up to 408 days after the main shock from a local network of five stations which became operational 20 days after the main shock. Their study showed that the Pisco earthquake triggered aseismic frictional afterslip on two adjacent patches, corresponding to the two main seismic asperities evidenced by *Sladen et al.* [2010]. The most prominent patch of afterslip coincides with the subducting Nazca ridge, an area also characterized by low interseismic coupling, which seems to have repeatedly acted as a barrier to seismic rupture propagation in the past.

Table 1. Horizontal Interseismic GPS Velocities Compiled by *Chlieh et al.* [2011] in a Stable South American Reference Frame[a]

Name	Longitude	Latitude	East	North	σEast	σNorth
CANA	−73.930	−13.990	5.71	2.11	2.40	1.50
CATA	−68.460	−16.300	−2.78	0.84	0.51	0.22
COMA	−68.440	−17.040	−0.86	6.53	1.60	1.50
HUAN	−75.210	−12.130	4.645	3.85	1.50	1.00
LEON	−67.600	−15.990	−7.15	5.18	1.50	1.10
PRAC	−76.360	−13.870	19.36	2.64	1.20	0.80
QUIL	−76.440	−12.950	18.63	3.96	2.10	1.20
REYE	−67.350	−14.300	−9.78	−0.12	3.60	2.00
SAPE	−67.420	−15.650	−6.11	1.11	2.00	1.90
SCRI	−77.020	−12.040	10.32	2.65	3.96	2.08
TANA	−74.450	−15.750	16.01	−0.67	3.10	2.20
ZAMA	−75.620	−14.660	14.04	2.22	3.50	2.30
LAND	−78.165	−12.168	38.66	4.39	5.19	5.53
SALI	−77.612	−11.238	21.21	1.78	7.09	4.01
SEAW	−78.486	−12.272	35.46	14.66	5.01	6.71

[a]Velocities and errors are expressed in mm/yr.

Here we revisit this previous study considering a larger observational time window using continuous GPS (cGPS) data from days 20 to 1204 after the main shock. We also use additional InSAR data to improve the spatial resolution of the model, in particular, the southward extension of afterslip. The coseismic and interseismic models are derived considering the same slab megathrust geometry, inversion method, boundary conditions, and slip azimuth as for the postseismic model to ensure a better consistency of the interseismic, coseismic, and postseismic models. This allows a better estimate of the contribution of each phase of the seismic cycle to the slip budget. Beyond a better characterization of the spatial evolution of afterslip, an important result of our study is the characterization of the onset of interseismic relocking of the principal seismic asperity that ruptured during the 2007 Pisco earthquake.

We start by presenting the data sets (InSAR and GPS) used in this study. We then describe the fault models and our inversion scheme before presenting the slip models for each phase (coseismic, postseismic, and interseismic) of the seismic cycle. We finally discuss the mechanical implications.

2. Data

2.1. Interseismic GPS Data

We use the GPS velocity field (15 sites) acquired between 1993 and 2003 [*Kendrick et al*., 2001; *Chlieh et al*., 2004; *Gagnon et al*., 2005] compiled in *Chlieh et al.* [2011]. These GPS data cover an area that extends from Lima region (latitude 11°S) in central Peru to southern Peru (latitude 17°S; see Figure 1). The description of the survey-mode GPS data and how they were expressed in the same reference frame can be found in *Chlieh et al.* [2011]. The interseismic GPS velocities presented in Table 1 are relative to a stable South American reference frame. This correction assumes an average rate of 4 mm/yr of the total convergence being accommodated by crustal shortening along the sub-Andean fold-and-thrust belt, a shortening rate consistent with previous geodetic estimates [*Bevis et al*., 2001; *Chlieh et al*., 2011], and with geological and paleomagnetic observations [*Kley and Monaldi*, 1998; *Arriagada et al*., 2008].

2.2. Coseismic InSAR Data

In this study we use four coseismic interferograms (Figure 2) that were processed and published by *Sladen et al*. [2010] (see Figures 2 and S1 in the supporting information). The coseismic InSAR data set is composed of one ascending ERS-2 image mode interferogram (track 447) formed from an acquisition 1 year prior to the earthquake and 2 days after the event and three ascending interferograms (tracks 109, 110, and 111) formed from image pairs acquired by the radar sensor on board the Japanese Space Agency (JAXA) satellite ALOS. The InSAR data span different time periods and include 2 to 6 weeks of postseismic deformation (Figure 2). As postseismic surface displacements measured by cGPS data are typically 1 order of magnitude smaller than coseismic displacements measured from InSAR (see Figures 3 and S1), we assume that the contribution of postseismic slip to the coseismic InSAR data is negligible.

A maximum line of sight (LOS) displacement of about 0.85 m is observed from ALOS interferogram acquired along track 111. The maximum InSAR LOS displacements observed from ERS-2 track 447 and ALOS track 110 interferograms are 0.55 and 0.40 m, respectively (see Figure S1).

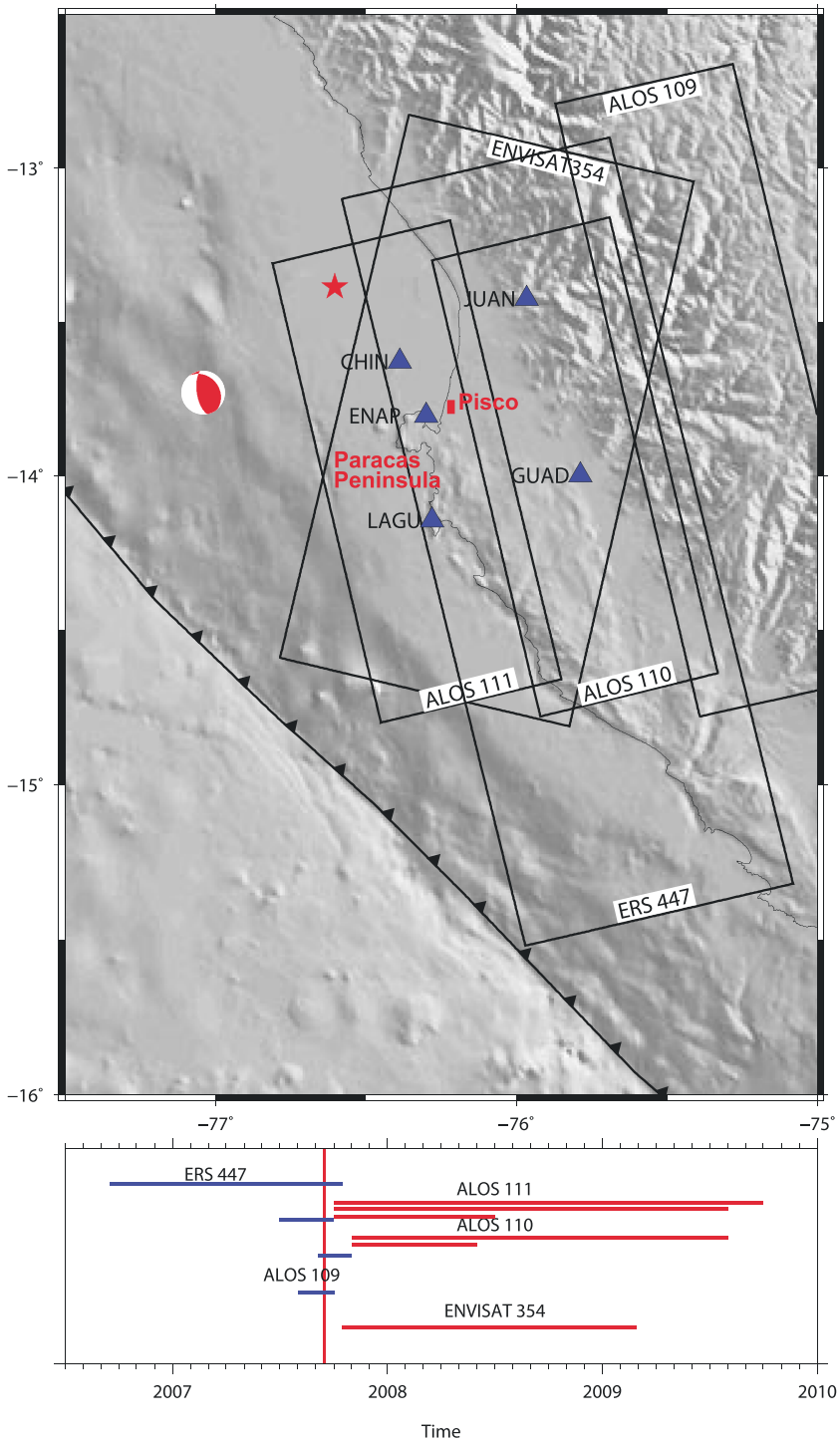

Figure 2. (top) GPS data and the coverage of the coseismic and postseismic InSAR data used in this study to determine the coseismic and postseismic slip distributions. Blue triangles show the location of the five cGPS stations used to measure and characterize the postseismic deformation. Black rectangles outline the spatial extent of the interferograms used in this study. The USGS location of the 2007 Pisco earthquake is shown as a red star, and the focal mechanism is from the global CMT catalog. (bottom) Time span covered by the InSAR images used for the inversion of coseismic displacement (in blue) and for the inversion of postseismic displacement (in red). The vertical red line indicates the time of the earthquake.

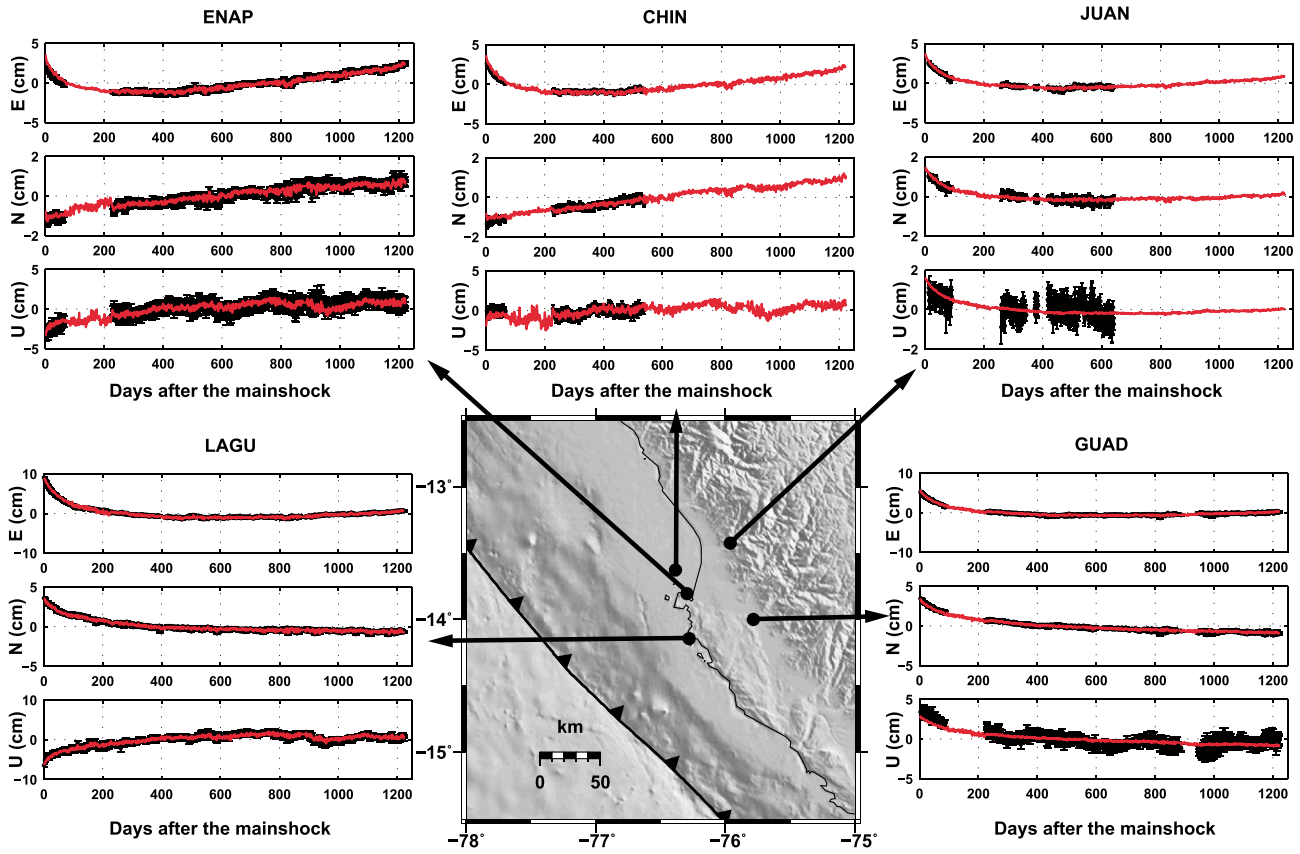

Figure 3. Postseismic displacement time series at the five GPS stations operating after the 2007 Pisco earthquake. Black dots with error bars are the observed GPS data with their 1σ uncertainty. Red lines show the predicted displacements for our best postseismic model. Note the clear reversal of displacements observed in the time series recorded at ENAP and CHIN at about 300 days (May 2008) after the main shock.

2.3. Postseismic GPS Data

Postseismic deformation was characterized from daily solutions at five cGPS stations, covering a time span of 3.5 years from days 20 to 1220 after the main shock (Figure 3). All five stations were operational by day 20 after the main shock. This data set covers a postseismic period about 3 times longer than in *Perfettini et al.* [2010]. Due to technical and logistical problems, some stations have ceased to operate during the observation period.

We performed the analysis of the cGPS data using the GAMIT/GLOBK software, version 10.5 [*Herring et al.*, 2010]. We completed the local network integrating data from regional and global International Global Navigation Satellite Systems Service network. This approach helps to decrease persistent noise and to stabilize the reference frame, especially because of the lack of observations west of the coastline. We performed the calculations using the International Terrestrial Reference Frame 2008 reference frame [*Altamimi et al.*, 2011] and determined positions with respect to a fixed South American plate. We paid a particular attention to integrate up-to-date modeling of environmental effects on the GPS measurements, such as tropospheric delay (mapping function and a priori pressure and temperature values from VMF1 [*Boehm et al.*, 2009] and ocean and atmospheric loading [*Tregoning and van Dam*, 2005; *Lyard et al.*, 2006]). This strategy efficiently decreases the noise level in the time series [*Vergnolle et al.*, 2010]. The 1σ accuracy of the daily positions is about 2.5 mm on the horizontal components and 5 mm on the vertical component. The network of cGPS stations provides a record of the temporal evolution of ground displacement following the Pisco earthquake (Figure 3). During the first 8 months, the direction of the horizontal motion observed at cGPS stations is clearly reverse compared to interseismic motion, indicating that postseismic displacements induced by the main shock clearly dominate the measured signal (Figure 3). The southernmost stations LAGU and GUAD recorded the maximum cumulative postseismic displacements of about 10 cm with LAGU showing 5 cm

uplift and GUAD 2.5 cm subsidence. After May 2008, the recorded displacement begins to vary depending on the station location. About 500 days after the main shock, the motion of the still operational stations ceases to be trenchward and reverse to inland motion, a feature that we interpret as the onset of interseismic motion in the area of the Pisco earthquake.

2.4. Postseismic InSAR Data

InSAR postseismic deformation was obtained considering two images from descending Envisat tracks (track 354) and 10 ALOS images from two ascending tracks (tracks 110 and 111; Figure 2). The differential interferograms were produced using the DIAPASON software [*©CNES/Altamira-information*, 1996] considering, for the Envisat interferograms, the precise orbit data from European Space Agency (ESA) Doppler orbitography and radiopositioning integrated by satellite, and for the ALOS interferograms, the orbit state vectors of their image header. The topographic contribution was removed subtracting the fringe pattern obtained from the 90 m posting digital elevation model generated from the Shuttle Radar Topography Mission. Next, a weighted power spectral density filter [*Goldstein et al.*, 1988] was used to filter the interferograms which were later unwrapped using an implementation of the network-flow algorithm for phase unwrapping [*Chen and Zebker*, 2002].

The subset of the interferogram data set shown in Figure 4 spans time intervals ranging from 1.5 to 2.5 years after the main shock (the full data set of interferograms used in this study is shown in Figure S2). The coherence is particularly low in the northern part of the Paracas Peninsula, mostly due to migrating coastal sand dunes. Consequently, InSAR data cannot provide any reliable information of the deformation field in this area. By contrast, all the independent interferograms are consistent in the south and beneath the peninsula. They show a phase variation with a coherent pattern in both space and time that provides an unambiguous observational evidence for postseismic deformation. The ascending Envisat interferogram (track 354) of Figure 4, formed from a pair of images acquired 2 months and 2 years after the main shock, shows a LOS displacement in the range of -5 to 3 cm, in which negative and positive signs mean displacement toward and away from the satellite, respectively. Similarly, the ALOS interferograms spanning 1 to 2 years of observation show a LOS displacement that may reach up to 12 cm of displacement toward the satellite. The spatial variability observed in Figure 4 is mainly explained by differences in acquisition geometry and by some atmospheric artifacts due to temporal variability of water vapor.

Each interferogram contains several million measurements of ground displacements in the LOS direction, a number too large to be considered in the inversion. Consequently, we downsampled each interferogram by averaging nearby pixels together resulting in a 500 m grid. This approach is justified because of the smoothness of the surface deformation field. As the spatial extent of a coherent area with no deformation in the study area is very limited, we were unable to constrain the full covariance structure. We assumed an uncorrelated uncertainty of 1 cm for Envisat data and 1.5 cm for ALOS data. The greater uncertainty associated with ALOS measurements was chosen to take into account the difference of the LOS range precision between L band and C band (1.6 to 4× worse than Envisat) [*Sandwell et al.*, 2008] and possible error contribution from the ionosphere.

3. Modeling Strategy

To model the surface deformation measured by InSAR and GPS related to the interseismic, coseismic, and postseismic stages, we assumed that it reflects only slip on the megathrust and that the surrounding medium is purely elastic. This modeling thus assumed that afterslip was the dominant mechanism responsible for postseismic ground deformation following the 2007 Pisco earthquake and ignore viscoelastic relaxation. We used the same fault geometry to perform the interseismic, coseismic, and postseismic slip distributions in order to ensure consistency between the different results. The goodness of the fit is quantified using the weighted root-mean-square of the residuals of both the GPS and InSAR data.

3.1. Fault Geometry

The fault surface was built considering that the location of the aftershocks occurred after the Pisco earthquake considering the U.S. Geological Survey–National Earthquake Information Center (USGS-NEIC) and interseismic coupling (ISC) catalogs together with the aftershocks from the local Instituto Geofísico del Perù network. The dip angle changes with depth, ranging from 6° at 5 km depth to 30° at about 50 km depth. For the coseismic and postseismic models, the fault plane extends 248 km along strike and 168 km in the downdip direction to reach beneath the coastline. The fault plane is discretized into 651 elementary patches of size $8 \times 8\,\mathrm{km}^2$. For the

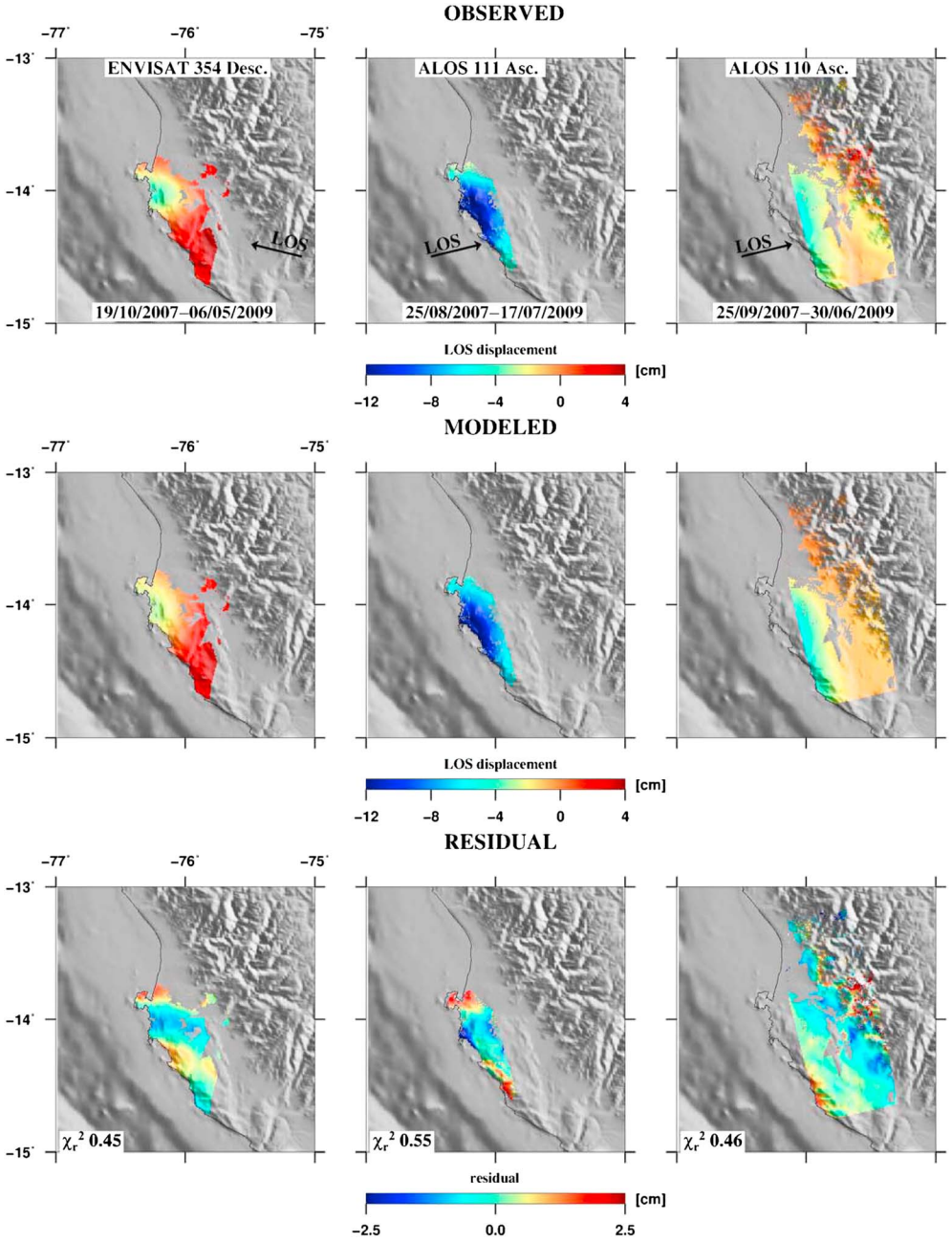

Figure 4. Observed and predicted postseismic interferograms for our best postseismic slip model. The satellite to ground radar line of sight (LOS) is shown with a black arrow. LOS displacements toward the satellite are negative (i.e., range decrease).

interseismic model, the along-strike dimension of the fault plane was extended to 720 km, ranging from 11 to 16.5°S latitude. The fault plane is composed of 611 patches discretized into $16 \times 16\,km^2$ elementary rectangles.

As in *Perfettini et al.* [2010], we tested a variety of slip models in which the slip azimuth was left free or fixed to the direction of plate convergence. We found that fixed azimuth slip models are able to properly match the data and have the advantage of reducing the number of degrees of freedom by 2, compared to variable azimuth models. Therefore, as done in *Perfettini et al.* [2010], we assume a fix slip azimuth of N250°E, corresponding to the direction of plate convergence, an assumption which further ensures consistency between the coseismic, postseismic, and interseismic slip models. This leads to a nearly constant rake value of about 70°, showing that the obliquity of the fault relatively to plate motion direction is constant in the study area. Note that for the interseismic model which uses the back slip approach [*Savage*, 1983], the slip azimuth is N70°E.

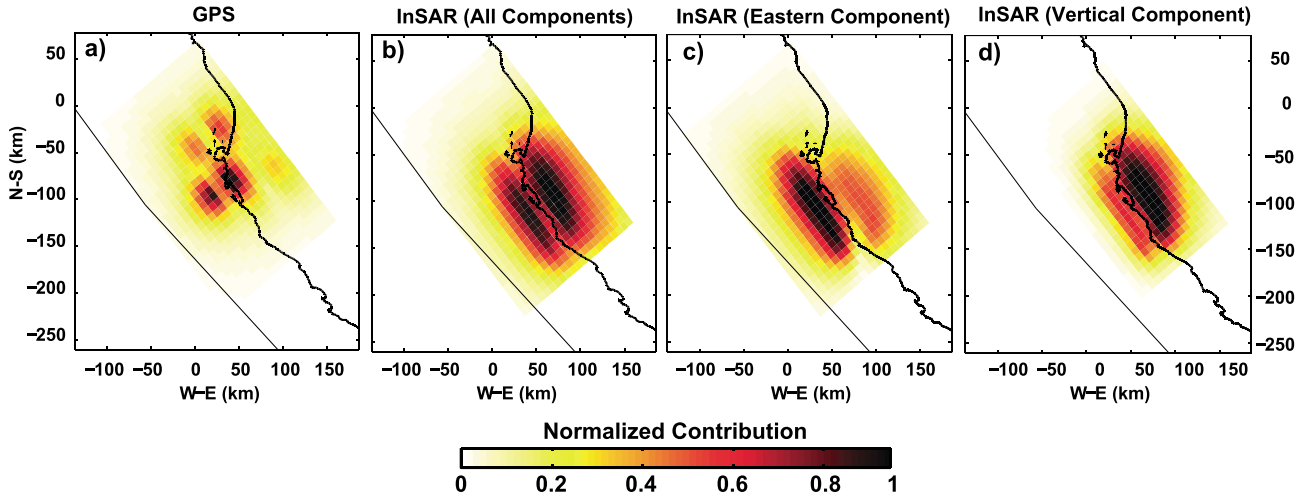

Figure 5. Spatial resolution of the postseismic models. Normalized contribution of each patch to the total displacement of postseismic GPS and InSAR observations assuming a homogeneous slip with an azimuth of N250°E, considering only (a) GPS observations and (b) InSAR observations. The low-resolution areas (value <0.1) are further used to constrain postseismic slip distributions (Figure 6) such that the slip on these areas is heavily penalized. (c) Same as in Figure 5b but considering only the eastern component of the InSAR observations. (d) Same as in Figure 5b but considering only the vertical component of the InSAR observations.

3.2. Resolution of the Inversions

A series of synthetic tests were performed to explore the spatial resolution of our inversions. To quantify the spatial resolution of our slip models, we computed the contribution of each patch to the total displacement of both the GPS and InSAR data sets [*Loveless and Meade*, 2011; *Perfettini and Avouac*, 2014]. The contribution of each patch is computed considering the cumulated displacement amplitude over all observation sites due a unit of slip on this given patch. We further normalized this field to have values between 0 and 1. The contribution of each patch to the postseismic model, considering the GPS and InSAR data, shows that the normalized contribution of the patches decreases away from land (Figure 5). Clearly, GPS stations improve the resolution significantly in their vicinity and the resolution at the southern part of the fault plane is better than at northern part. When considering separately the eastern and vertical components of the InSAR observations, the patches located near the coast contribute strongly to the eastern motion rather than shallower patches contribute greater to the vertical motion (Figures 5c and 5d).

The spatial resolution of our models was further tested with additional resolution tests where we imposed an initial slip distribution consisting of a collection of circular asperities (35 km for postseismic models and 70 km for the interseismic one) with unit slip to test the ability of our model to recover the imposed pattern (Figures S3a–S3c and Text S2 in the supporting information), considering various values of the smoothing parameter. In agreement with Figure 5, the postseismic model shows a lower ability to recover the imposed slip pattern in the northwestern part of the fault plane, even using a low value (rough model) of the smoothing parameter γ.

3.3. Principal Component Analysis-Based Inversion Method Decomposition

The GPS time series were next decomposed using the principal component analysis-based inversion method (PCAIM) initially proposed by *Kositsky and Avouac* [2010]. PCAIM allows the reduction of large data sets by decomposing the data into a limited number of components, thereby naturally removing data noise while significantly reducing the inversion computing time. Furthermore, unlike the classical principal component decomposition, PCAIM is able to manage unevenly sampled time series and to properly take into account data uncertainties. The methodology is described in detail in the PCAIM manual (http://www.tectonics.caltech.edu/resources/pcaim/) and has been used in a number of studies [*Lin et al.*, 2010; *Perfettini et al.*, 2010; *Bedford et al.*, 2013; *Gualandi et al.*, 2013; *Perfettini and Avouac*, 2014; *Remy et al.*, 2014; *Thomas et al.*, 2014].

The daily GPS time series are stored in a $M \times N$ matrix X_{dat}, where $M = 3n_{stat}$ and $N = n_{meas}$, n_{stat} being the number of stations and n_{meas} the number of measurements epochs, the factor 3 in the definition of M corresponding to the number of displacement directions (east, north, and vertical). In the case of the postseismic

phase of the Pisco earthquake, X_{dat} is a 15×1204 matrix. The decomposition algorithm in PCAIM returns the matrices U, S and V, U_k and V_k being unit vectors, such that

$$X_{svd} = \sum_{k=1}^{n_{comp}} U_k S_k V_k^t \quad (1)$$

where the upper index $(\ldots)^t$ means the matrix transpose and n_{comp} is the number of components considered in the decomposition. The vector U_k of length M is only space dependent, while the vector V_k of length n_{meas} is only time dependent, S_k being a scalar quantifying the fraction of the data variance explained by each component. We computed the reduced chi-square χ_r^2 of the residual between the matrix X_{dat} and X_{svd} to measure the accuracy of the PCAIM decomposition using the following formulation:

$$\chi_r^2 = \frac{1}{M \times N} \sum \left[\frac{X_{dat} - X_{svd}}{\sigma} \right]^2 \quad (2)$$

where X_{svd} is the reconstructed data matrix and $\boldsymbol{\sigma}$ is the GPS data standard uncertainties. From the analysis of the variation of χ_r^2 with the number of components (Figure S4), only four components are necessary to reconstruct the original cGPS data.

3.4. Inversion Scheme

For postseismic models the slip distribution L in elastic medium is related to the surface displacements through

$$X_{dat} = GL \quad (3)$$

where G is the Green's function operator that gives the displacement at the measuring sites resulting from a unit slip applied on each patch of the fault. To compute the Green's functions, we consider rectangular dislocations embedded in a homogeneous elastic half-space [*Okada*, 1992], assuming a Poisson coefficient of 0.25. As in *Perfettini et al.* [2010], we estimate moments considering a shear modulus of 50 GPa. After writing equation (1) in a compact matricial form and combining it with equation (3), we obtain

$$L = \left(G^{-1}U\right)SV^t \quad (4)$$

In the PCAIM algorithm, we solve for

$$\begin{pmatrix} C_u' U \\ 0 \end{pmatrix} = \begin{pmatrix} C_u' G \\ \gamma \Delta \end{pmatrix} m \quad (5)$$

C_u' being obtained from the Cholesky decomposition so that $C_u'^t C_u' = C_u^{-1}$, where C_u is the covariance matrix of U. The Laplacian matrix Δ is a smoothing operator (see the PCAIM manual for details) regularizing the inversion and γ the associated smoothing parameter; m ($2 \times$ number of dislocations $\times n_{comp}$) is the slip on the fault. To account for the lack of resolution of the model (section 3.2), slip is penalized in all models for which the normalized contribution of Figure 5 is lower than 0.1. This is done in practice by setting the Laplacian Δ to 0 for the concerned patches.

The final slip distribution is obtained combining equations (4) and (5) yielding

$$L = m\, SV^t \quad (6)$$

In equation (4), the eigenvectors U and V of the decomposition are obtained considering the cGPS dense data set. In the case of the Pisco earthquake, InSAR data are considered as a sparse data set due to their temporal scarcity and are included as additional constraints to equation (5) (see section 2.8 of the PCAIM manual for details). In the joint inversion with GPS and InSAR data, each data set was weighted according to their uncertainty. InSAR data can suffer from spatially long-wavelength orbital or atmospheric errors. Due to the limited spatial extent of coherent area with no deformation it was not possible to estimate the orbital contribution outside the deforming region. It was also not possible to estimate orbital uncertainties by analyzing differences between measurements made by GPS and by InSAR due to the limited number of stations lying inside the radar scenes. Therefore, we decided to augment the linear system (equation (5)) to include the coefficients of a linear ramp in space for each interferogram. We preferred using a two-dimensional linear ramp correction rather than a quadratic or high-order ramp corrections in order to reduce the trade-off between fault slip and ramp parameters.

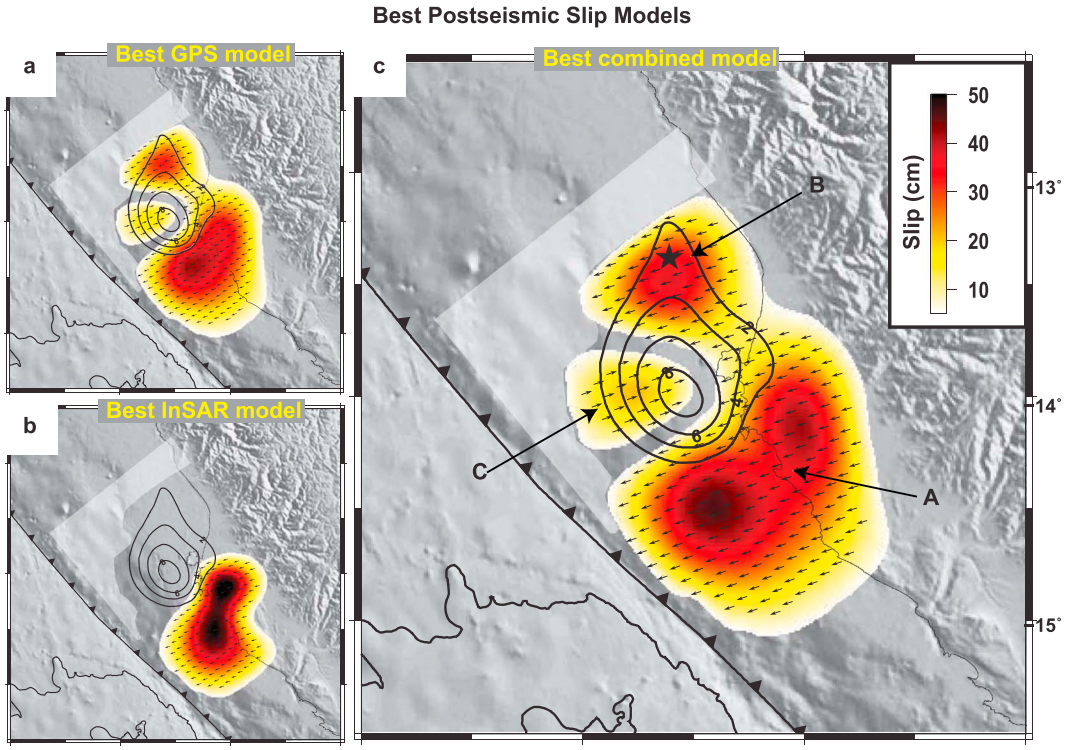

Figure 6. Best postseismic slip distribution model inferred from cGPS and InSAR data. (a) Using GPS data alone. (b) Using InSAR data alone. (c) Using GPS and InSAR data simultaneously. The light gray transparent area represents the low-resolution area of Figure 5.

4. Results

We have explored extensively the sensitivity of our coseismic, postseismic, and interseismic models to model parameters. Text S4 shows a wider range of models obtained considering various smoothing constraints. As discussed in section 3.4, slip is penalized in all slip models within low-resolution areas (section 3.2) as well as on the lateral and bottom fault edges.

4.1. Coseismic Slip Distribution

Our preferred coseismic model (Figure 6c and Text S5 for additional details) shows a single asperity of high slip (up to 10 m) located offshore the Paracas Peninsula at 20 km depth, very similar to the one proposed by *Pritchard and Fielding* [2008]. It is also similar to the source model proposed by *Sladen et al.* [2010] which differs in that it shows two slip patches, one close to the epicenter location and the second larger one in the same area as our peak slip. The difference is probably due to the use of the seismological waveforms by *Sladen et al.* [2010], which requires two distinct seismic asperities. The estimated geodetic moment of our model is 1.8×10^{21} Nm corresponding to M_w8.1 assuming a shear modulus of 50 GPa. Our moment estimate is larger than the global centroid moment tensor (CMT) solution (i.e., 1.1×10^{21} Nm) and the solution of *Biggs et al.* [2009] (i.e., 1.06×10^{21} Nm) but comparable with those obtained by other previous studies ranging from 1.20×10^{21} [*Sladen et al.*, 2010] to 1.91×10^{21} Nm [*Pritchard and Fielding*, 2008].

4.2. Postseismic Slip Distribution

From the inversion, we obtained different possible postseismic slip models depending on the data set used: the cGPS data alone, the InSAR data alone, and the combined GPS/InSAR data sets (Figures 6a–6c). The light gray transparent region in Figure 6 corresponds to the low-resolution area where slip is penalized. The afterslip model of Figure 6a based on the GPS data alone is very good and yields $\chi_r^2 = 0.7$. This model shows two major slip zones of afterslip: a large region located south of the Paracas Peninsula (hereinafter named A) and another one located north of the peninsula, near the epicenter (hereinafter named B). Those two patches of afterslip were previously evidenced by *Perfettini et al.* [2010], considering cGPS data acquired from days 20 to 408.

A major difference with the results of *Perfettini et al.* [2010] is that it is not possible to fit the cGPS data using an afterslip model considering only forward (trenchward) slip. Afterslip in the backward direction is required to fit the reversal from seaward to landward displacements recorded in the 1200 days of GPS time series (Figure 3) and corresponding to a return to interseismic motion. This explains the presence of a patch with slip reversal (referred to as region C hereafter) located near the region of high coseismic slip. Considering the nonuniqueness of the underdetermined inversion problem, we tested the robustness of this feature imposing additional constraints on the slip distribution. This analysis, presented in Text S6, leads to the conclusion that slip reversal is required by the GPS data as indicated by the behavior of the V_2 eigenvector (see Text S3 and Figure S5) and does not result from a lack of resolution.

Our preferred slip model of Figure 6b based on the InSAR data alone well adjusts the data yielding $\chi^2_r = 0.6$. It shows a single region of significant afterslip corresponding to region A. The amount of slip is comparable to the model based on the GPS data only, although slightly larger. Note that the existing difference is not significant and depends on the particular choice of the smoothing parameter. Due to the lack of resolution of the InSAR-based model in the northern part of our study area (related to the large zone affected by phase decorrelation), no slip is derived neither in regions B nor C.

When considered simultaneously, the InSAR and GPS data fit equally well the observations than when considered individually, yielding $\chi^2_r = 0.73$, highlighting the consistency between the two data sets (Text S1 in the supporting information). A similar slip model was obtained by inversion without correcting from a linear ramp, but the residual between InSAR observations and modeled displacements is greater $(\chi^2{}_r = 2.4)$, showing that slip inversion is strongly constrained by the GPS measurements. This model (Figure 6c) resembles in patch A the GPS-alone-based model (Figure 6a) while sharing the feature of the InSAR-alone-based model. In both the GPS- and InSAR-based inversions, the areas of large afterslip are located in regions peripheral to the coseismic rupture zone. This pattern is consistent with the notion that afterslip is driven by the main shock stress changes [e.g., *Perfettini and Avouac* 2004a, 2004b]. The inferred postseismic slip distribution is mostly located at a depth shallower than 40 km, suggesting that its origin is more consistent with afterslip in the seismogenic zone than by viscous flow in the deep ductile zone. In principle, deep afterslip trades off with viscoelastic relaxation [*Sun and Wang*, 2015] so that the amount of deep afterslip (along the coastline) estimated from our model could be overestimated.

Figures 7b–7d provide a synthetic view of the time evolution of slip (counted positive in the forward direction consistent with the long-term slip on the megathrust) at three representative zones of the fault plane for our preferred model (Figure 6c). The evolution of slip on those selected patches is computed for three roughness values encompassing 3 orders of magnitude of the smoothing parameter (see Figure S7). The smoother model poorly explains the data as demonstrated by the poor fit of this model, yielding χ^2 of ~5 (Figure S7c). For the smoother model, slip in regions B and C vanish due to the large amount of smoothing applied. By contrast, afterslip motion is observed on patch A, confirming that aseismic slip predominates over this fault segment. Both the rougher and optimal models (blue and magenta curves of Figure 7b) fit the data well, leading to $\chi^2 = 0.43$ and 0.73, respectively. For those models, the temporal evolution of slip depends on the degree of smoothness used. For both models, a linear trend is observed at patch C but its onset depends on the smoothing parameter, varying from about 100 to 300 days. Nevertheless, this linear trend observed at patch C is about 60 mm/yr (see the dashed lines in Figure 7b), a value close to the plate convergence rate (61 mm/yr) in this region. Consequently, these models imply a full relocking of the asperity that ruptured during the 2007 Pisco earthquake.

4.3. Interseismic Slip Distribution

We estimate interseismic coupling (ISC) which quantifies the degrees of fault locking considering interseismic velocities obtained before the main shock. ISC is defined as

$$\mathrm{ISC}(x) = 1 - \frac{V_{\mathrm{inter}}\ (x)}{V_L}, \tag{7}$$

where x is the current location, V_L is the long-term fault slip rate, and V_{inter} is the slip rate distribution during the interseismic period. A value of 1 means that the fault is fully locked, requiring that the accumulated stress is released by transient slip events such as earthquakes. Such areas are interpreted to be governed by patches with rate-weakening frictional properties, promoting slip instabilities. A value of 0 corresponds to a creeping region, governed by rate-strengthening frictional properties. An intermediate value might correspond to regions that are composed of a mixture of rate-weakening and rate-strengthening regions or areas located in the stress shadow of major asperities [*Bürgmann et al.*, 2005].

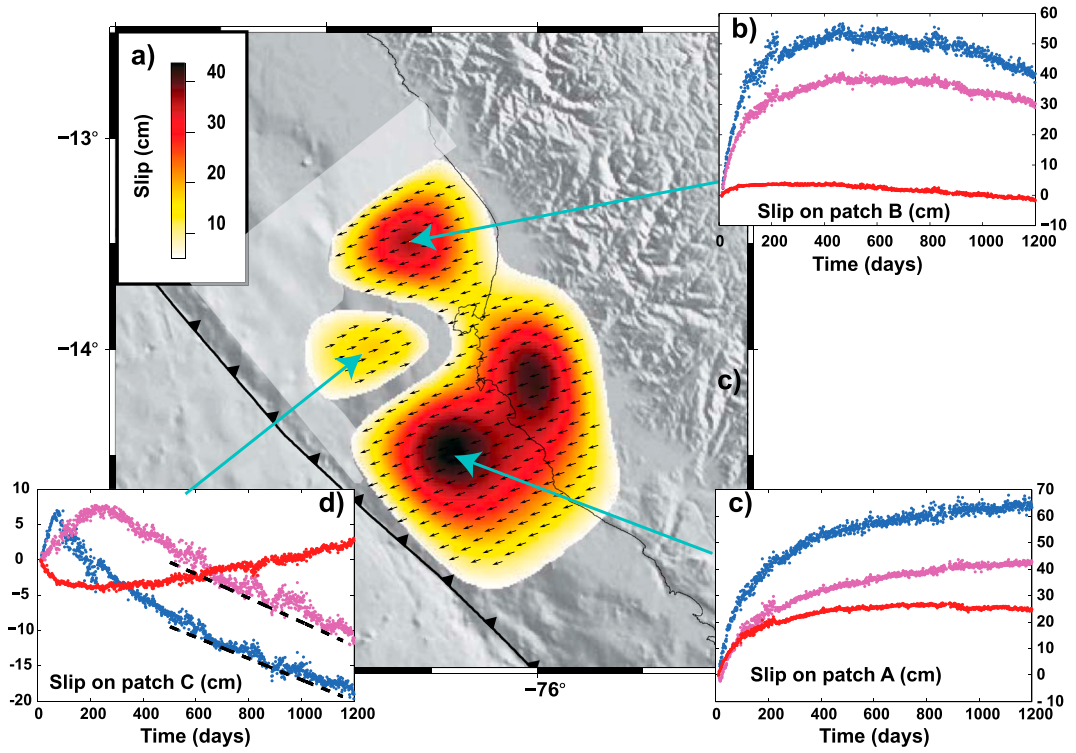

Figure 7. (a) Preferred postseismic model. (b) Slip at the center of region B from the rougher (in blue), the best fitting (in purple), and the smoother (in red) models, respectively. (c) Slip at the center of region A with same color code as in Figure 7b. (d) Slip at the center of the back slip region C with same color code as in Figure 7b. Dashed lines correspond to a 60 mm/yr linear trend, equal in magnitude to the long-term slip rate on the megathrust. We interpret the slip reversal as evidence for relocking of that patch. Vector indicates the displacement of the hanging wall with respect to the footwall.

The slip rate distribution normalized assuming a plate convergence rate of 61 mm/yr was obtained considering a smoothing parameter of $\gamma = 2.5$ (Figure 8). This value of the smoothing parameter offers a good compromise between the model roughness and the misfit to the data (see Text S4 for a detailed explanation). As shown in Figure 8, the model fits well the GPS data with a $\chi_r^2 = 0.4$, indicating a good agreement between the model predictions (black vectors) and the observations (white vectors). This model is close to the models of *Perfettini et al.* [2010] and *Chlieh et al.* [2011], even if the megathrust geometry used in this study slightly differs from the one used in these previous studies. The Pisco earthquake occurred at the edge of an area with an ISC close to 1, consistent with the picture that the region of significant coseismic slip was mostly locked prior to the main shock. The Nazca ridge, where the 2007 Pisco rupture stopped, coincides also well with an area of low ISC, consistent with the idea that this large structure is essentially creeping and plays the role of a permanent strong barrier to large earthquakes.

In Figure 8, the green vectors show the estimated horizontal velocity computed at ENAP, LAGU, and GUAD using the long-term linear trends estimated from days 500 to 1200 after the main shock (Figure 3). The velocity observed at ENAP is consistent with the preearthquake value observed at the neighboring station PRAC (distant by only a few kilometers), suggesting that station ENAP is back to a motion characteristic of the interseismic period. No similar conclusion can be drawn for LAGU and GUAD, as no preearthquake velocities exist for these points.

5. Discussion

5.1. Return to the Interseismic Phase and Relocking of the Rupture Zone

The three stations still in operation by the end of the analyzed period (ENAP, LAGU, and GUAD) show a reversal from westward to eastward displacements around day 500 after the main shock (Figure 3), followed by a linear trend suggesting a return to interseismic motion. In the rough and optimal slip models that fit the data well, slip reversal is observed on patch C, roughly in the area of maximum coseismic slip. A linear trend is observed in region C, but its onset time depends on the degree of smoothing of the model. It can be as early

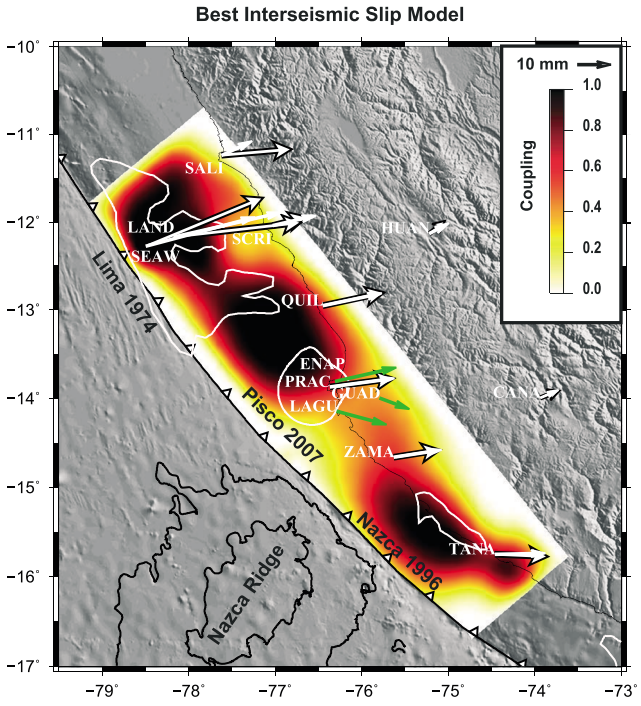

Figure 8. Best interseismic coupling model. Black and white arrows show the observed and predicted interseismic GPS velocities, respectively. The observed interseismic velocities are those determined by *Kendrick et al.* [2003] expressed in the stable South American reference frame using the Euler pole of *Chlieh et al.* [2011]. Note that no preearthquake interseismic velocities are available at GUAD and LAGU. The green arrows show the estimated horizontal velocity computed at ENAP, LAGU, and GUAD with observations ranging from days 500 to 1200 after the main shock.

as 100 days for the rough model and as late as 300 days for our optimal model, showing that the precise time for the onset of this linear motion is not resolvable by the inversion process. One remarkable feature is that the slope of the linear trend observed in patch C is unaffected by the smoothness of the model, yielding a long-term velocity of 60 mm/yr, a value in close agreement with the regional plate convergence rate of 61 mm/yr. This remarkable closeness demonstrates that the onset of a linear trend corresponds to a return to an interseismic motion. Region C corresponding roughly to the rupture area of the Pisco earthquake (Figure 6), this return to interseismic motion can be seen as a relocking of the rupture zone after the main shock.

The relocking time is not resolvable but increases with the smoothness of the model (Figure 7). Since no GPS data were available before day 20 after the main shock, we cannot resolve a relocking time smaller than 20 days in any case. The fact that the region affected by this return to interseismic motion closely matches the rupture area of the Pisco earthquake strongly suggests that region C was a locked region in the interseismic period that only moves coseismically. Although not resolvable in this study, we believe that the relocking time could be very small and even null, corresponding to a complete relocking right after the coseismic as observed for the asperity that slipped during the 2003 Chengkung earthquake in Taiwan [*Thomas et al.*, 2014].

5.2. Frictional Properties of the Interface

Between days 20 and 1204, about 60 cm of slip accumulated on patch A. Both the behavior of the slip distribution and the amplitude of cumulated slip are consistent with the results of *Perfettini et al.* [2010], obtained between days 20 and 408. Not surprisingly, our inferred cumulated slip is higher than *Perfettini et al.* [2010] as we consider a larger time period in this study. The time evolution of postseismic slip on patch A (Figure 9c) increases as the logarithm of time, consistent with the idea that afterslip is governed by rate-strengthening friction with a logarithmic dependency on slip rate [*Marone et al.*, 1991; *Perfettini and Avouac*, 2004a].

In the steady state approximation, and assuming that the creeping velocity just before the coseismic stress change applied is equal to the long-term slip rate V_{pl}, the observed time evolution of afterslip should be consistent with frictional afterslip modeled considering a velocity-strengthening rate and state friction law [*Perfettini and Avouac*, 2004b]

$$V_L t_r \log\left[1 + d\left(\exp\left(\frac{t}{t_r}\right) - 1\right)\right] \tag{8}$$

where V_L is the long-term velocity rate (fixed to 61 mm/yr), d is the velocity jump due to the main shock, t_r is the relaxation time associated with frictional afterslip, and t is the time after the main shock. Figure 9c shows the prediction of equation (8). The model (black continuous line) matches well the evolution of slip (blue dots) in region A, for a relaxation time $t_r = 2.26$ years and a coseismic velocity jump $d = 188$.

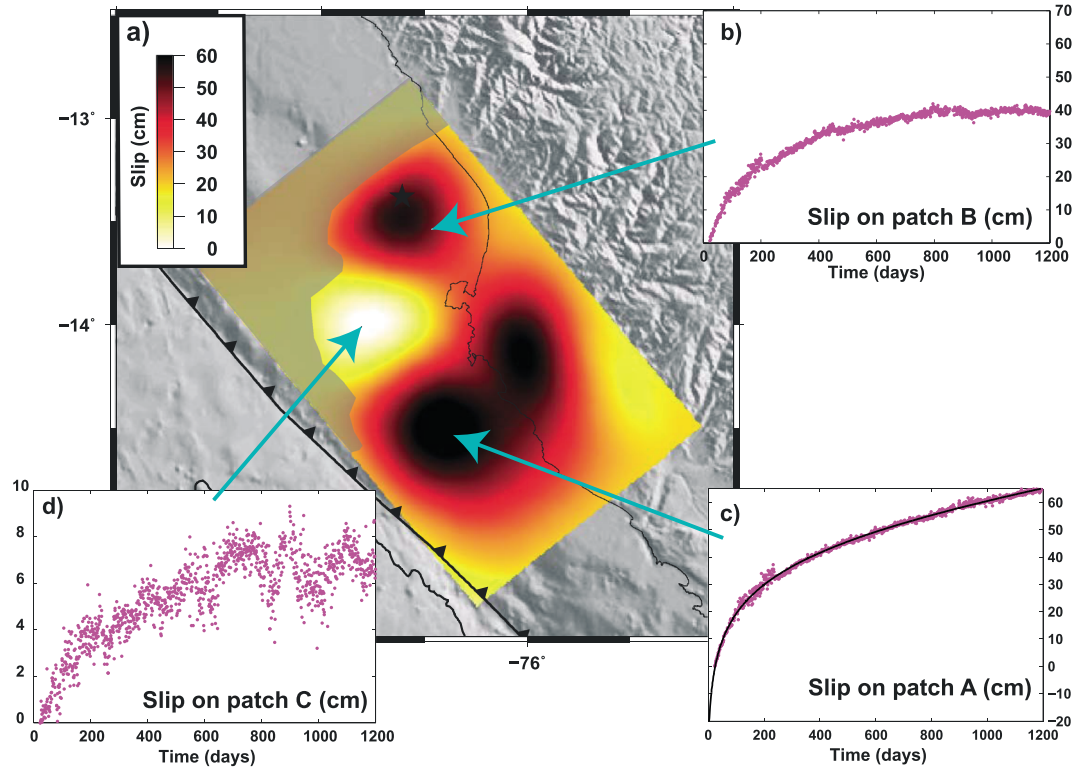

Figure 9. Same as in Figure 8 but after subtracting to fault slip the linear slip velocity observed at patch C. The continuous black line in Figure 8c shows the theoretical displacements predicted from a rate-strengthening frictional sliding defined by the equation (8).

The slip evolution observed on patch B (Figure 7b) is clearly different from the one observed on patch A. After about 500 days of decaying afterslip, the patch returns gradually to an interseismic motion as observed at patch C (see section 5.1). Normalizing the time series (see Figure S11) shows that the temporal evolution at sites B and C is similar and that only the slip amplitude is different, site B showing a larger amount of afterslip. The fact that sites B and C show an initial phase of afterslip before returning to complete locking is understandable if one imagines that both patches are mostly composed of rate-weakening materials (promoting seismic rupture) with some rate-strengthening patches within (promoting aseismic slip). Those creeping patches were strongly loaded by the main shock and released this excess of stress through afterslip. Once unloaded, they returned to interseismic loading, but because they are mostly surrounded by locked brittle patches, the creep rates are close to zero due to the stress shadows of those brittle asperities [*Bürgmann et al*., 2005; *Hetland and Simons*, 2010]. Since B shows a greater amount of afterslip, it is expected that the ratio of strengthening versus weakening patches is higher there than at C, this ratio being small anyway in order for the patch to move seismically. The opposite is observed at site A that is expected to have a ratio-strengthening versus rate-weakening patch close to 1, so that site A is essentially creeping (but some minor seismicity corresponding to the rupture of the isolated weakening patches within A could still be observed).

The initiation of the rupture of the Pisco earthquake having occurred nearly at the center of patch B supports the idea that this site is mostly rate weakening. The fact that the afterslip in B was significantly larger than in C is consistent with a lower coseismic slip in B than in C (see Figure 6 and *Sladen et al.* [2010]), B containing a higher fraction of creeping patches than at site C. Note that this whole reasoning relies on the reasonable assumption that the frictional properties of the interface are heterogeneous at scales much smaller than our resolution scale (typically of a few tenths of kilometers).

5.3. Slip Budget and Recurrence Time

The various slip models derived for the coseismic, postseismic, and interseismic phases can be used to quantify the contribution of each phase to the final budget of the seismic cycle. For the coseismic models

of Figure S6, the seismic moments corresponding to the rough, optimal, and smooth models yield, respectively, $M0_{cos} = 1.99 \times 10^{21}$, 1.81×10^{21}, and 1.74×10^{21} Nm, corresponding to moment magnitudes of 8.13, 8.10, and 8.09, respectively. Those values are larger than the value of M_w8.0 found by *Sladen et al.* [2010] considering InSAR and teleseismic data, possibly because we have chosen a too large depth-averaged shear modulus (50 GPa). If we use a shear modulus of 35 GPa (a value consistent with the depth average of the velocity model of *Sladen et al.* [2010]), we find a seismic moment of 1.27×10^{21} yielding $M_w = 8.0$, meaning that the slip potency of our model is close to the estimate of *Sladen et al.* [2010].

As discussed in section 6, the linear trends observed in the postseismic models at the end of our observation period (Figure 7) are interpreted as a return to interseismic motion. Its existence allows for a precise determination of the slip deficit rate in the rupture zone, more accurate than the preearthquake coupling model of Figure 8 that it is less well constrained because based on sparser GPS campaign data and no InSAR data. Consequently, we used the moment deficit rate determined in the relocking zone of region C. For the rough, optimal, and smooth models of Figure 7, those moment deficit rates are, respectively, $dM0_{inter}/dt = 1.08 \times 10^{19}$, 1.07×10^{19}, and 1.02×10^{19} Nm/yr.

For consistency with the estimate of the interseismic moment deficit rates, the moment of the postseismic models are estimated considering the model of Figure 9 for which the slip distribution has been corrected from the linear contribution observed at region C, resulting in zero slip in this region. This postseismic slip distribution can be seen as the net contribution of afterslip, corrected from the interseismic reloading. For the rough, optimal, and smooth models, the postseismic moments are, respectively, $M0_{post} = 2.39 \times 10^{20}$, 2.06×10^{20}, and 1.46×10^{20} Nm. Note that those values are comparable to the estimate of 1.73×10^{20} Nm found by *Perfettini et al.* [2010] ranging from 9×10^{19} to 3×10^{20} Nm, meaning that most afterslip accumulated before day 408 (the last observation day of *Perfettini et al.* [2010]).

The return period T_{rec} of an event similar to the Pisco earthquake can be estimated using

$$T_{rec} = \frac{M0_{cos} + M0_{post}}{dM0_{inter}/dt} \tag{9}$$

yielding $T_{rec} = 218$ years for our optimal model and, respectively, $T_{rec} = 174$ years and 188 years for our rough and smooth models. These values are consistent, although smaller, than what could be expected knowing that the last large event in this area struck in 1746.

Our estimate of the postseismic moment corresponds to the observation period covering days 20 to 1204. We show in Text S7 that the postseismic moment from days 0 to 1204 can be taken into account by increasing the postseismic moment by a factor of 1.37, yielding postseismic moments of $M0_{post} = 3.27 \times 10^{20}$, 2.82×10^{20}, and 2.00×10^{20} Nm for the rough, optimal, and smooth models, respectively. Using equation (9) with those updated values gives $T_{rec} = 180$, 227, and 195 years, for the rough, optimal, and smooth models, respectively, those values being in closer agreement with the observed elapsed time of 261 years. The optimal value of 227 years is different from the estimate of 250 years obtained by *Perfettini et al.* [2010], who determined the slip deficit rate in the rupture zone using a preearthquake coupling model similar to our model of Figure 8.

The previous estimates of the coseismic and postseismic models allow determining the ratio of postseismic versus coseismic moments. Using $M0_{cos} = [1.99, 1.81, 1.74] \times 10^{21}$ Nm and $M0_{post} = [3.27, 2.82, 2.00] \times 10^{20}$ Nm (rough, optimal, and smooth models, respectively), we find that the postseismic moment from days 0 to 1204 of our optimal model represents 0.16 of the coseismic moment but can vary from 0.1 to 0.19 considering the end-member (i.e., rough and smooth) models. Those values are about twice smaller than the range of 22–41% found in *Perfettini et al.* [2010]; these differences are mostly due to our estimate of the postseismic moment. Those estimates are similar to other major subduction earthquakes for which this ratio has been estimated [*Lin et al.*, 2013, and references therein].

We estimated the cumulative moment released by all aftershocks with $M_w > 4$ reported in the NEIC earthquake catalog over the same time period. We find that aftershocks released about 1.5×10^{19} Nm, representing between 4.6 and 7.5% of the moment released by the distribution of net afterslip, suggesting a predominantly aseismic process.

The average contribution of coseismic slip to the long-term slip budget is [*Perfettini et al.*, 2010]

$$C_{cos} = \mathrm{ISC}(1 + \alpha)^{-1} \tag{10}$$

where α is the ratio of the postseismic and coseismic moments. The contribution of the postseismic creep to the slip budget writes

$$C_{\text{post}} = \frac{\alpha}{1+\alpha}\text{ISC} \tag{11}$$

while the contribution of the interseismic creep is, by definition,

$$C_{\text{inter}} = 1 - \text{ISC} \tag{12}$$

The contribution $C_{\text{aseismic}} = C_{\text{inter}} + C_{\text{post}}$ of aseismic creep to the cycle is then

$$C_{\text{aseismic}} = 1 - \text{ISC}(1+\alpha)^{-1} \tag{13}$$

where we have assumed that $C_{\text{cos}} + C_{\text{inter}} + C_{\text{post}} = 1$, neglecting aseismic transients other than afterslip. Aseismic transients might exist and have been observed elsewhere along this subduction zone, but in absence of reliable constraints for this area, we have decided to neglect them.

According to the estimates given earlier in this section, $\alpha = 0.16$ for our optimal model but $0.1 < \alpha < 0.19$ considering all range of acceptable models. In region C, the mean ISC is 0.55 for the rough model and 0.52 for the optimal model. Using equation (13) yields $C_{\text{aseismic}} = 0.55$ for our preferred models but $0.5 < C_{\text{aseismic}} < 0.56$ considering all acceptable models. This means that, in the area of the Pisco earthquake, about 55% of the slip budget in the 0–50 km depth range is aseismic. Those values fall in the lower range $0.49 < C_{\text{aseismic}} < 0.71$ previously proposed by *Perfettini et al.* [2010].

The seismological waveforms of the Pisco earthquake clearly indicated two distinct ruptures [*Sladen et al.*, 2010], separated by 60 s of seismic silence. This delay might correspond to the time needed to nucleate the second rupture, or alternatively to an aseismic rupture occurring within the region connecting the two asperities, similar to the rupture of tsunami earthquakes. Indeed, the asperities being distant by roughly 60 km, 60 s of delay would roughly give a rupture velocity on the order of 1 km/s, a value consistent with tsunami earthquakes but too low for regular earthquakes [*Lay et al.*, 2010].

Even if those scenarios remain speculative, we can still attempt to account for a possible contribution of aseismic slip to the total coseismic moment. Let us call $f_{\text{post}} \approx 0.16$ the ratio of our estimated postseismic and coseismic moments. The coseismic moment is defined as $f_{\text{cos}} {M_0}^{\text{cos}}$, where $f_{\text{cos}} \approx 1.4$ and ${M_0}^{\text{cos}}$ corresponds to the estimate of *Sladen et al.* [2010] obtained considering teleseismic data, so that ${M_0}^{\text{cos}}$ represents the moment due to seismic waves. Let us further assume that this difference is purely due to aseismic slip, then the fraction $(f_{\text{cos}} - 1){M_0}^{\text{cos}}$ corresponds to aseismic coseismic slip and/or early afterslip that could have happened during the 20 days following the main shock and during which our GPS network was not yet operational. Consequently, the ratio of moment released by aseismic slip to the coseismic moment (as derived from seismology) could be as large as $f_{\text{cos}} \times f_{\text{post}} + (f_{\text{cos}} - 1) \approx 0.62$, with the possibility of a fraction of this aseismic slip happening early enough to have contributed to the tsunami.

6. Conclusion

Our study shows that the main asperity that ruptured during the 2007 Pisco earthquake relocked soon after the earthquake while afterslip occurred in its peripheral area with a relaxation time estimated to about 2.3 years. The relocking time cannot be resolved accurately though.

We show that slip at the center of the region of maximum afterslip, along which the Nazca ridge is subducting (region A), is consistent with rate-strengthening friction promoting aseismic creep, consistent with the interseismic coupling model that shows a low coupling. The value of the relaxation time suggests that postseismic relaxation is over now and that the creep rate in that area has returned to its preearthquake value. Our postseismic moment represents about 16% of the coseismic moment, a value smaller than the previous estimate of *Perfettini et al.* [2010], and the main reason for this discrepancy being that our coseismic moment estimate is larger than in *Sladen et al.* [2010].

The interseismic model of Figure 8 is in agreement with the results of *Perfettini et al.* [2010] and *Chlieh et al.* [2011], both showing that the Nazca ridge corresponds to a low coupling region, consistent with the hypothesis that the region is essentially creeping and acts as an aseismic barrier to large earthquakes.

Aseismic slip might account for 50% of the long-term slip in the 0–50 km depth range, a value corresponding to the lower bound given by *Perfettini et al.* [2010]. The return period of an earthquake of M_w8.1 in the Pisco area is estimated at 227 years, assuming that the interseismic strain derived in this study is constant during the seismic cycle.

Comparison of the coseismic, postseismic, and interseismic slip distributions suggest that seismic slip and afterslip occur, respectively, in regions of high ($>$0.5) and low ISC ($<$0.5) values. The coseismic and postseismic slip distributions complement one another, consistent with the notion that afterslip occurs in regions strongly loaded by the main shock. Finally, those results suggest that the frictional properties of the interface are permanent during the seismic cycle.

Acknowledgments

ASAR data were provided by the European Space Agency (ESA) through the project Envisat-AO857 and category 1 2899. PALSAR data from the ALOS satellite mission operated by the Japanese Aerospace Exploration Agency (JAXA) were used under the terms and conditions of the fourth ALOS 2 Research Announcement (project 1142). This work was supported by the Institut de Recherche pour le Développement (IRD). We thank the people from Laguna Grande village for their great support. We thank Nino Puma Sacsi for this precious help in maintaining station LAGU operational and Alberto Zheimer for supporting the network from day 70 to day 220. Some of the figures were prepared using the GMT software [*Wessel and Smith*, 1991]. The data for this paper are available by contacting the corresponding author at remy@ird.fr. We thank Lisa Christiansen for editing the text. The Assistant Editor and an anonymous reviewer provided useful and constructive remarks that greatly improved this study.

References

©CNES/Altamira-information (1996), Philosophie et mode d'emploi de la chaîne logicielle interférométrique DIAPASON, Toulouse, France.

Altamimi, Z., X. Collilieux, and L. Métivier (2011), ITRF2008: An improved solution of the international terrestrial reference frame, *J. Geod.*, *85*, 457–473.

Arriagada, C., P. Roperch, C. Mpodozis, and P. R. Cobbold (2008), Paleogene building of the Bolivian Orocline: Tectonic restoration of the central Andes in 2-D map view, *Tectonics*, *27*, TC6014, doi:10.1029/2008TC002269.

Bedford, J., et al. (2013), A high-resolution, time-variable afterslip model for the 2010 Maule M_w = 8.8, Chile megathrust earthquake, *Earth Planet. Sci. Lett.*, *383*, 26–36.

Bevis, M., E. Kendrick, R. Smalley, B. Brooks, R. Allmendinger, and B. C. Isacks (2001), On the strength of interplate coupling and the rate of back arc convergence in the central Andes: An analysis of the interseismic velocity field, *Geochem. Geophys. Geosyst.*, *2*, 1067, doi:10.1029/2001GC000198.

Biggs, J., D. P. Robinson, and T. H. Dixon (2009), The 2007 Pisco, Peru, earthquake (*M*8.0): Seismology and geodesy, *Geophys. J. Int.*, *176*, 657–669.

Boehm, J., J. Kouba, and H. Schuh (2009), Forecast Vienna Mapping Functions 1 for real-time analysis of space geodetic observations, *J. Geod.*, *83*, 397–401.

Bürgmann, R., M. G. Kogan, G. M. Steblov, G. Hilley, V. E. Levin, and E. C. B. Apel (2005), Interseismic coupling and asperity distribution along the Kamchatka subduction zone, *J. Geophys. Res.*, *110*, B07405, doi:10.1029/2005JB003648.

Chen, C. W., and H. A. Zebker (2002), Phase unwrapping for large SAR interferograms: Statistical segmentation and generalized network models, *IEEE Trans. Geosci. Remote Sens.*, *40*, 1709–1719.

Chlieh, M., et al. (2007), Coseismic slip and afterslip of the Great (M_w9.15) Sumatra-Andaman earthquake of 2004, *Bull. Seismol. Soc. Am.*, *97*, S157–S173, doi:10.1785/0120050631.

Chlieh, M., J. B. de Chabalier, J. C. Ruegg, R. Armijo, R. Dmowska, J. Campos, and K. Feigl (2004), Crustal deformation and fault slip during the seismic cycle in the North Chile subduction zone, from GPS and InSAR observations, *Geophys. J. Int.*, *158*, 695–711.

Chlieh, M., H. Perfettini, H. Tavera, J.-P. Avouac, D. Remy, J.-M. Nocquet, F. Rolandone, F. Bondoux, G. Gabalda, and S. Bonvalot (2011), Interseismic coupling and seismic potential along the central Andes subduction zone, *J. Geophys. Res.*, *116*, B12405, doi:10.1029/2010JB008166.

Dorbath, L., A. Cisternas, and C. Dorbath (1990), Assessment of the size of large and great historical earthquake in Peru, *Bull. Seismol. Soc. Am.*, *80*, 551–576.

Gagnon, K., C. D. Chadwell, and E. Norabuena (2005), Measuring the onset of locking in the Peru-Chile trench with GPS and acoustic measurements, *Nature*, *434*, 205–208.

Goldstein, R. M., H. A. Zebker, and C. L. Werner (1988), Satelite radar interferometry: Two dimensional phase unwrapping, *Radio Sciences*, *23*, 713–720.

Gualandi, A., E. Serpelloni, and M. E. Belardinelli (2013), Space-time evolution of crustal deformation related to the M_w 6.3, 2009 L'Aquila earthquake (central Italy) from principal component analysis inversion of GPS position time-series, *Geophys. J. Int.*, *197*, 174–191.

Herring, T. A., R. W. King, and S. C. McClusky (2010), *Introduction to GAMIT/GLOBK. Release 10.4*, Dep. of Earth, Atmos. Planet. Sci. Mass. Inst. Technol, Cambridge, Mass. [Available at http:/www.gpsg.mit.edu/~simon/gtgk/doc.htms.]

Hetland, E. A., and M. Simons (2010), Post-seismic and interseismic fault creep II: Transient creep and interseismic stress shadows on megathrusts, *Geophys. J. Int.*, *181*, 99–112.

Ioualalen, M., H. Perfettini, S. Y. Condo, C. Jimenez, and H. Tavera (2012), Tsunami modeling to validate slip models of the 2007 M_w 8.0 Pisco earthquake, central Peru, *Pure Appl. Geophys.*, *170*, 433–451.

Kendrick, E., M. Bevis, R. Smalley, and B. Brooks (2001), An integrated crustal velocity field for the central Andes, *Geochem. Geophys. Geosyst.*, *2*, 1066, doi:10.1029/2001GC000191.

Kendrick, E., M. Bevis, R. Smalley, B. Brooks, R. B. Vargas, E. Lauría, and L. P. Souto Fortes (2003), The Nazca–South America Euler vector and its rate of change, *J. South Am. Earth Sci.*, *16*, 125–131.

Kley, J., and C. R. Monaldi (1998), Tectonic shortening and crustal thickness in the central Andes: How good is the correlation?, *Geology*, *26*, 723–726.

Kositsky, A. P., and J.-P. Avouac (2010), Inverting geodetic time series with a principal component analysis-based inversion method, *J. Geophys. Res.*, *115*, B03401, doi:10.1029/2009JB006535.

Langer, C. J., and W. Spence (1995), The 1974 Peru earthquake series, *Bull. Seismol. Soc. Am.*, *85*, 665–687.

Lay, T., C. Ammon, R. Hutko, and H. Kanamori (2010), Effects of kinematic constraints on teleseismic finite-source rupture inversion: Great Peruvian earthquakes of 23 June 2001 and 15 August 2007, *Bull. Seismol. Soc. Am.*, *100*, 969–994.

Lin, Y. N., A. P. Kositsky, and J.-P. Avouac (2010), PCAIM joint inversion of InSAR and ground-based geodetic time series: Application to monitoring magmatic inflation beneath the Long Valley Caldera, *Geophys. Res. Lett.*, *37*, L23301, doi:10.1029/2010GL045769.

Lin, Y. N., et al. (2013), Coseismic and postseismic slip associated with the 2010 Maule earthquake, Chile: Characterizing the Arauco Peninsula barrier effect, *J. Geophys. Res. Solid Earth*, *118*, 3142–3159, doi:10.1002/jgrb.50207.

Loveless, J., and B. Meade (2011), Spatial correlation of interseismic coupling and coseismic rupture extent of the 2011 M_w = 9.0 Tohoku-oki earthquake, *Geophys. Res. Lett.*, *38*, L17306, doi:10.1029/2011GL048561.

Lyard, F., F. Lefevre, T. Letellier, and O. Francis (2006), Modelling the global ocean tides: Modern insights form FES2004, *Ocean Dyn.*, doi:10.1007/s10326-006-0086-x.

Marone, C. J., C. H. Scholtz, and R. Bilham (1991), On the mechanics of earthquake afterslip, *J. Geophys. Res.*, *96*, 8441–8452.

Moreno, M., M. Rosenau, and O. Oncken (2010), 2010 Maule earthquake slip correlates with pre-seismic locking of Andean subduction zone, *Nature*, *467*, 198–202.

Motagh, M., R. Wang, T. R. Walter, R. Bürgmann, E. Fielding, J. Anderssohn, and J. Zschau (2008), Coseismic slip model of the 2007 August Pisco earthquake (Peru) as constrained by wide swath radar observations, *Geophys. J. Int.*, *174*, 842–848.

Okada, Y. (1992), Internal deformation due to shear and tensile faults in a half-space, *Bull. Seismol. Soc. Am.*, *82*, 1018–1040.

Perfettini, H., and J.-P. Avouac (2004a), Postseismic relaxation driven by brittle creep: A possible mechanism to reconcile geodetic measurements and the decay rate of aftershocks, application to the Chi-Chi earthquake, Taiwan, *J. Geophys. Res.*, *109*, B02304, doi:10.1029/2003JB002488.

Perfettini, H., and J.-P. Avouac (2004b), Stress transfer and strain rate variations during the seismic cycle, *J. Geophys. Res.*, *109*, B06402, doi:10.1029/2003JB002917.

Perfettini, H., and J. P. Avouac (2014), The seismic cycle in the area of the 2011 M_w9.0 Tohoku-Oki earthquake, *J. Geophys. Res. Solid Earth*, *119*, 4469–4515, doi:10.1002/2013JB010697.

Perfettini, H., et al. (2010), Seismic and aseismic slip on the central Peru megathrust, *Nature*, *465*, 78–81.

Pritchard, M. E., and E. J. Fielding (2008), A study of the 2006 and 2007 earthquake sequence of Pisco, Peru, with InSAR and teleseismic data, *Geophys. Res. Lett.*, *35*, L09308, doi:10.1029/2008GL033374.

Pritchard, M. E., and M. Simons (2006), An aseismic slip pulse in northern Chile and along-strike variation in seismogenic behavior, *J. Geophys. Res.*, *111*, B08405, doi:10.1029/2006JB004258.

Pritchard, M. E., E. O. Norabuena, C. Ji, R. Boroschek, D. Comte, M. Simons, T. H. Dixon, and P. A. Rosen (2007), Geodetic, teleseismic, and strong motion constraints on slip from recent southern Peru subduction zone earthquakes, *J. Geophys. Res.*, *112*, B03307, doi:10.1029/2006JB004294.

Remy, D., J. L. Froger, H. Perfettini, S. Bonvalot, G. Gabalda, F. Albino, V. Cayol, D. Legrand, and M. D. Saint Blanquat (2014), Persistent uplift of the Lazufre volcanic complex (central Andes): New insights from PCAIM inversion of InSAR time series and GPS data, *Geochem. Geophys. Geosyst.*, *15*, 3591–3611, doi:10.1002/2014GC005370.

Sandwell, D. T., D. Myer, R. Mellors, M. Shimada, B. Brooks, and J. Foster (2008), Accuracy and resolution of ALOS interferometry: Vector deformation maps of the Father's Day intrusion at Kilauea, *IEEE Trans. Geosci. Remote Sens.*, *46*, 3524–3534.

Savage, J. C. (1983), A dislocation model of strain accumulation and release at a subduction zone, *J. Geophys. Res.*, *88*, 4984–4996.

Sladen, A., H. Tavera, M. Simons, J. P. Avouac, A. O. Konca, H. Perfettini, L. Audin, E. J. Fielding, F. Ortega, and R. Cavagnoud (2010), Source model of the 2007 M_w 8.0 Pisco, Peru earthquake: Implications for seismogenic behavior of subduction megathrusts, *J. Geophys. Res.*, *115*, B02405, doi:10.1029/2009JB006429.

Subarya, C., M. Chlieh, L. Prawirodirdjo, J.-P. Avouac, Y. Bock, K. Sieh, A. J. Meltzner, D. H. Natawidjaja, and R. McCaffrey (2006), Plate-boundary deformation associated with the great Sumatra-Andaman earthquake, *Nature*, *440*, 46–51.

Sun, T., and K. Wang (2015), Viscoelastic relaxation following subduction earthquakes and its effects on afterslip determination, *J. Geophys. Res. Solid Earth*, *120*, 1329–1344, doi:10.1002/2014JB011707.

Thomas, M. Y., J.-P. Avouac, J. Champenois, J.-C. Lee, and L.-C. Kuo (2014), Spatiotemporal evolution of seismic and aseismic slip on the Longitudinal Valley Fault, Taiwan, *J. Geophys. Res. Solid Earth*, *119*, 5114–5139, doi:10.1002/2013JB010603.

Tregoning, P., and T. van Dam (2005), Atmospheric pressure loading corrections applied to GPS data at the observation level, *Geophys. Res. Lett.*, *32*, L22310, doi:10.1029/2005GL024104.

Vergnolle, M., A. Walpersdorf, V. Kostoglodov, P. Tregoning, J. A. Santiago, N. Cotte, and S. I. Franco (2010), Slow slip events in Mexico revised from the processing of 11 year GPS observations, *J. Geophys. Res.*, *115*, B08403, doi:10.1029/2009JB006852.

Wessel, P., and W. H. F. Smith (1991), Free software help map and display data, *Eos Trans. AGU*, *72*(41), 441–446, doi:10.1029/90EO00319.